Influence of the anode buffer layer materials and the light radiation power on the efficiency of a planar p-i-n perovskite solar cell: theory and simulation

Bita Farhadi,[a] **Fatemeh Zabihi**,[b] **Mike Tebyetekerwa**,[c] **Ishaq Lugoloobi**,[b] **and Aimin Liu**[a,*]
[a]Dalian University of Technology, School of Physics and School of Microelelctronics, Dalian, China
[b]Donghua University, College of Materials Science and Engineering, State Key Laboratory for Modification of Chemical Fibers and Polymer Materials, Shanghai Belt and Road Joint Laboratory of Advanced Fibers and Low-Dimension Materials, Shanghai, China
[c]The University of Queensland, School of Chemical Engineering, St. Lucia, Brisbane, Queensland, Australia

Abstract. Planar perovskite solar cell (PSC) measuring 900 nm total thickness is designed and simulated using Silvaco and SCAPS. Silvaco (Atlas 5.16.3.R) photovoltaic simulating system enables the formation of the stacking model and estimation of the physical properties of various functional materials, whereas SCAPS (version. 3.3.07) patterns the photovoltaic metrics including the fill factor (FF), power conversion efficiency (PCE), open-circuit voltage (*Voc*), short-circuit current density (*Jsc*), maximum voltage (*Vm*), maximum current (*Im*), absorption and reflection coefficients, and energy state diagram of the whole device. Alternation of illumination power and use of different buffer materials was utilized as the main tuning strategy. The champion layout was achieved by optimization of the stacking model, material system, and power of illumination, which demonstrated 26.32% PCE, 83.77% FF, *Jsc* of 26.27 $\mathrm{mA/cm^2}$, and the exceptional *Voc* of 1.19 V. This theoretical performance remains stable in 1000 $\mathrm{W/m^2}$ light radiation. The calculated efficiency and FF were very close to the previously reported experimental data, and this proved the high accuracy of this simulation work. These findings promise a feasible application of PSC in high-efficiency wearable electronics. *© 2022 Society of Photo-Optical Instrumentation Engineers (SPIE)* [DOI: 10.1117/1.JPE.12.015503]

Keywords: solar cell; perovskites; reflection; absorption; radiation; buffer layer.

Paper 21084G received Oct. 19, 2021; accepted for publication Feb. 15, 2022; published online Mar. 1, 2022.

1 Introduction

Perovskite solar cells (PSCs) are nearly changing the game in the energy market, as they are attaining the efficiencies of their commercial counterparts.[1,2] However, the intermittence over time and climate conditions still make them unreliable for commercial applications. Moreover, the bulk and molecular imperfections and mismatches of the work function in different junctions keep the genuine power conversion efficiency (PCE) of PSCs lag behind the theoretical values.[3] Plenty of configurations, stacking manners, and material systems have been surveyed experimentally, but the results have not exceeded ~25% PCE,[4] which is yet standing far below the predicted potential of 31.4% PCE.[3]

From a technical point of view, the performance and lifetime of a perovskite multijunction, especially where an organic–inorganic composition is used, are dramatically disturbed by numerous internal and external potential triggers. Light intensity and the power of illumination, humidity, external environmental temperature, and the number, thickness, contact, and quality of the junctions, as well as the intrinsic physical properties of each layer, such as thermal and electrical resistivity, light absorption-reflection behavior and thermal and chemical stability,

---

*Address all correspondence to Aimin Liu, aiminl@dlut.edu.cn

1947-7988/2022/$28.00 © 2022 SPIE

all together rule out the net performance and durability of PSCs. In addition to the above factors, materials such as composites and atomic-doped materials, rearrangement of stacking orders, engineering of interfaces, addition of protective, heat sucking, and antirefractive layers are also known to greatly affect the overall PCE performance of PSCs.[1–11] It is therefore necessary to develop and generalize the systematic protocols for addressing these factors in terms of optimization, for improved cell efficiency.

The experimental studies however are highly informative but are designed for a limited domain of conditions, and hard to be reproduced plainly. Having a numerical/theoretical backup minimizes the data points and saves time, costs, hazards, and the related systematic errors. Nonetheless, there has been so far less attention to the theoretical works on perovskite materials and their related electronic devices. Some simulation works have been done to explore the effect of using different materials, changing cell layer thickness, and the effect of defect densities. For example, Lakhdar et al. simulated a PSC with SCAPS software, in which they studied and designed the effects of electron transporting layer (ETL) on the Ge-based PSC for an improved performance. They used different materials as ETL, among which the PSC with C_{60} illustrated the highest PCE of 13.5% compared with those with other ETL materials.[12] In another work, Chowdhury et al. investigated the effects of defect density on the absorber layer and n/i interface for PSCs using the SCAPS software. Based on the simulation results, a PCE of $>25\%$ was reported with a fill factor (FF) of 85%. They concluded that by increasing the absorber layer thickness, the efficiency increased rapidly. And that the defect density has a great effect on the PSC, which can be overcome by increasing the thickness of the perovskite layer.[13,14] Also, Malyukov et al. presented a numerical model for the simulation of a PSC. The simulation results showed that the thickness of the perovskite absorber layer and its qualities (charge carrier lifetime and diffusion length) can significantly affect PSC efficiency.[15] Many other similar works can be found in the literature, including those focusing on absorber layer thickness,[14,16–18] defect density, and doping concentration.[17,19,20]

Solar harvesting potential is the focal point of the current article. For the light-harvesting and photovoltaic materials particularly, plenty of interactive factors are potentially confining their level and ability of harvesting light energy. The atomic and crystalline nature of the photovoltaic materials, as well as the position and area of exposure, day-time, and the weather condition, are reasons for the serious malfunction in any given photovoltaic device.[21–25]

In this work, we dually address the light-harvesting shortcomings in a planar p-i-n PSC. From one side, a range of organic and inorganic photoanode substances, i.e., titanium dioxide (TiO_2), zinc oxide (ZnO), phenyl-C_{61}-butyric acid methyl ester (PCBM), and tin (IV) oxide (SnO_2) (ETL materials), are adopted as ETLs, and the performance of the issuing devices is compared. From the other side, different powers of illumination after exposure to light are monitored and discussed in a meaningful trend. For the simulation results with Silvaco, we first defined the mesh structure, followed by the materials and thickness of each layer, and thereafter their doping concentration and type. Then we defined the contacts and biased the structure under $AM_{1.5}$ light illumination, to earn the mesh structure, potential distribution in each layer, recombination rate, and net doping of the proposed structure. With the SCAPS software, we designed the proposed structure and defined material properties and defect density for each layer and biased the structure with 1.5V-voltage under different illumination powers. Then, we changed the hole transporting layer (HTL) and ETL thickness and materials, and the buffer layer materials and investigated their effects. All the simulations were done with Gummel and Newton Raphson methods. $MAPbI_3$ was selected as the model photovoltaic material, and copper oxide (Cu_2O), copper thiocyanate (CuSCN), and Spiro-OMeTAD materials were separately used as the HTLs, whereas P_3HT, zinc telluride (ZnTe), and cadmium telluride (CdTe) were incorporated and compared as the buffer layers. With all the above-mentioned setups, optimization works confirmed that a p-i-n planar PSC can potentially yield over 26% PCE, with the optimal ETL, HTL, buffer layer, optical traits of the photovoltaic layer, and the thickness while keeping a proper power exposure to light.[26–28]

2 Simulation Parameters

For the simulation work and calculation of parameters, we applied both Silvaco and SCAPS for programming. Silvaco is based on the digital resolution of the three fundamental equations of

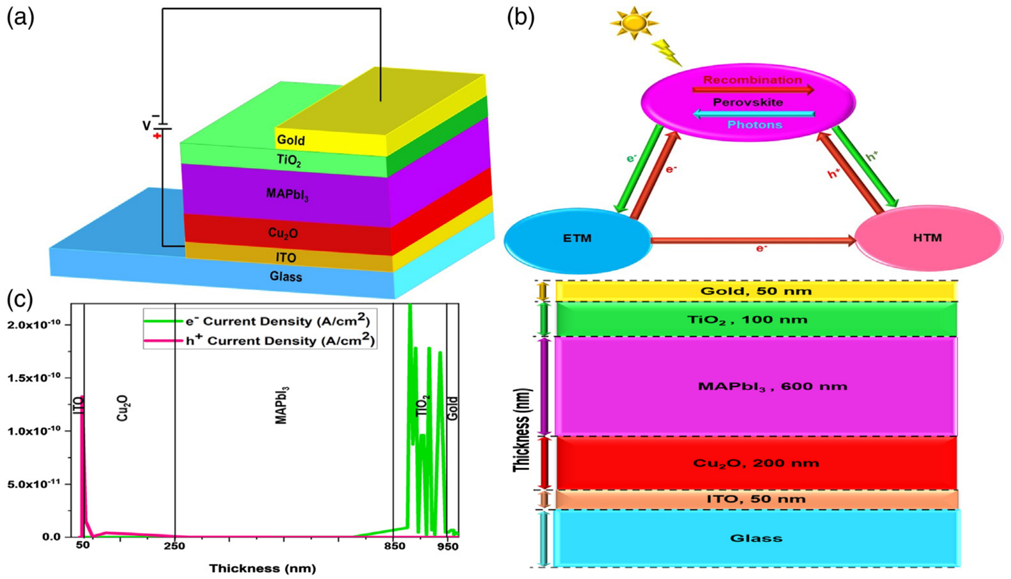

Fig. 1 Schematic view of the (a) hypothetical alignment of the highly efficient PSC and (b) charge transfer path. (c) Electrons' and holes' current density distribution in various thicknesses of the proposed structure. (ETM, electron transfer materials; HTM, hole transfer materials).

charge transport in semiconductors; these are continuity and transport equations for electrons, holes, and Poisson's equations.[29] SCAPS on the other hand calculates the current–voltage characteristics, energy bands, and spectral response (quantum efficiency), by solving continuity equations for electron, hole, and Poisson's equation.[30] Figures 1(a) and 1(b) show the schematic view of the hypothetical alignment and charge carrier transfer pathway of PSC, respectively. While the distribution of the electron and hole current density in different photovoltaic and selective layers is shown in Fig. 1(c), for the designed PSC based on TiO_2 and Cu_2O as ETL and HTL, respectively. Table 1 tabulates the physical and optical properties of the materials in different layers, as theoretically estimated for the architecture shown in Fig. 1. As observed, a 50-nm ITO film as the front electrode, a 200-nm Cu_2O as HTL, a 600-nm $MAPbI_3$ PV film, a 100-nm

Table 1 Physical and electrical properties of the materials used in the proposed structure.

Materials	Cu_2O[28]	$MAPbI_3$[31]	TiO_2[27]
Electron affinity (eV)	3.20	3.75	3.90
Electron mobility μ_e (cm^2/V_s)	200	2	20
Hole mobility μ_h (cm^2/V_s)	80	2	10
Band gap energy E_g (eV)	2.17	1.55	3.20
Conduction band effective density of states N_C (cm^{-3})	$2.-02 \times 10^{17}$	2.20×10^{15}	1.00×10^{21}
Valence band effective density of states N_V (cm^{-3})	1.10×10^{19}	2.20×10^{17}	2.00×10^{20}
Dielectric constant $\varepsilon/\varepsilon_0$	7.11	6.50	9
Acceptor concentration N_A (cm^{-3})	1.00×10^{18}	1.00×10^{15}	—
Donor concentration N_D (cm^{-3})	—	1.00×10^{15}	1.00×10^{18}
Defect density N_t (cm^{-3})	1.00×10^{15}	2.30×10^{13}	1.00×10^{15}

TiO_2 as ETL, and a 50-nm gold as the top contact form an ultrathin two-dimensional PSC, in which the carrier densities of $1 \times 10^{15}\ \mathrm{cm}^{-3}$ (p-type), $1 \times 10^{15}\ \mathrm{cm}^{-3}$ (n-type), and $1 \times 10^{18}\ \mathrm{cm}^{-3}$ (n-type) are created in the HTL, ETL, and PV layers, respectively, upon illumination.

In Fig. 1(b), the green arrows show the ideal direction for energy conversion, including photon excitation, electron transfer from the perovskite layer to the ETL, and hole transfer from the perovskite layer to the HTL. Also, the red arrows indicate the energy lost during delivery to the charge carriers. Such a parasitic effect includes recombination and leakage or backward flow of electrons and holes from the ETL and HTL, respectively, to the perovskite layer. The rate and mechanism of these phenomena are dominated by the state of the energy profile in the whole system. In detail, part of the dissipated energy depends on the bandgap of $MAPbI_3$, and the level of conformity between the valance band of HTL and the conduction band of ETL with respect to $MAPbI_3$. On the other hand, the ratio between the absorbed and the total incident photons should be kept as high as possible. It means that the chances of reflection or transmission from the PV layer will be minimized.[32–36]

Figure 1(c) shows the density of hole and electron obtained upon illumination in various functional layers, through simulation backed up with the following equations:

$$J_p = -q\mu_p p\nabla(\phi - \phi_p) + KT\mu_p\nabla_p, \tag{1}$$

$$J_n = -q\mu_n n\nabla(\phi - \phi_n) + KT\mu_n\nabla_n, \tag{2}$$

where Jp is the current density due to the mobility of holes, Jn is the current density due to the mobility of electrons, μ_n is the electron mobility, μ_p is the hole mobility, q is the electron charge, ϕ is the electrostatic potential, and K is the Boltzmann's constant.

3 Results and Discussion

3.1 *Recombination Rate in Functional Layers*

Generation or production of excited electron–holes and charge carriers concurrently from the valance band of the semiconductor to the conduction band requires a sufficient amount of energy (larger than the bandgap of the material) from photons or other resources. This leaves a hole in the valance band. Recombination with an inverse mechanism includes a relaxation mode in which electrons and holes reunite in the valance band and then are annihilated. The latter process is associated with energy production in the form of heat or radiation. In a balanced status, the rate of recombination and generation are equal. For specific applications such as solar cells and light-emitting diodes (LEDs), this equation should be canceled. For the solar cells, a minor rate of recombination is desired, and in LEDs, a high range of radiating recombination is required.[37–41]

Herein, we estimated the rate of recombination through the PV and charge selective layers of the proposed PSC, and calculations were performed based on different mesh constructions. Figures 2(a)–2(d) compare the profile of recombination rate in different layers, with and without the boundary conditions. Figures 2(e) and 2(f) correspondingly demonstrate the forms of the mesh structure, without and with consideration of the boundary conditions. It is observed that when the boundary conditions are put into the calculation system, the rate of recombination through the cell increases to more than two orders of magnitude. This is well in line with reality as the boundary conditions theoretically define the interfaces and junctions of ETL and HTL with the PV layer. In a practical case, these interfaces are the key points of recombination based on two main reasons: first, for the offsets of valance band at HTL/PV and conduction bands at PV/ETL; second, because of the inevitable bulk and crystalline defections at the borders that can trap the carrier and exhaust their energy, pushing them back to the valance band of the photovoltaic layer.[1,3] Moreover, in polycrystalline structures such as perovskite films, the mesh density presents the frequency of grain boundaries, which in the normal case could be in the range of 10^{10} to 10^{20} orders of magnitude.[1,3,8,42–44]

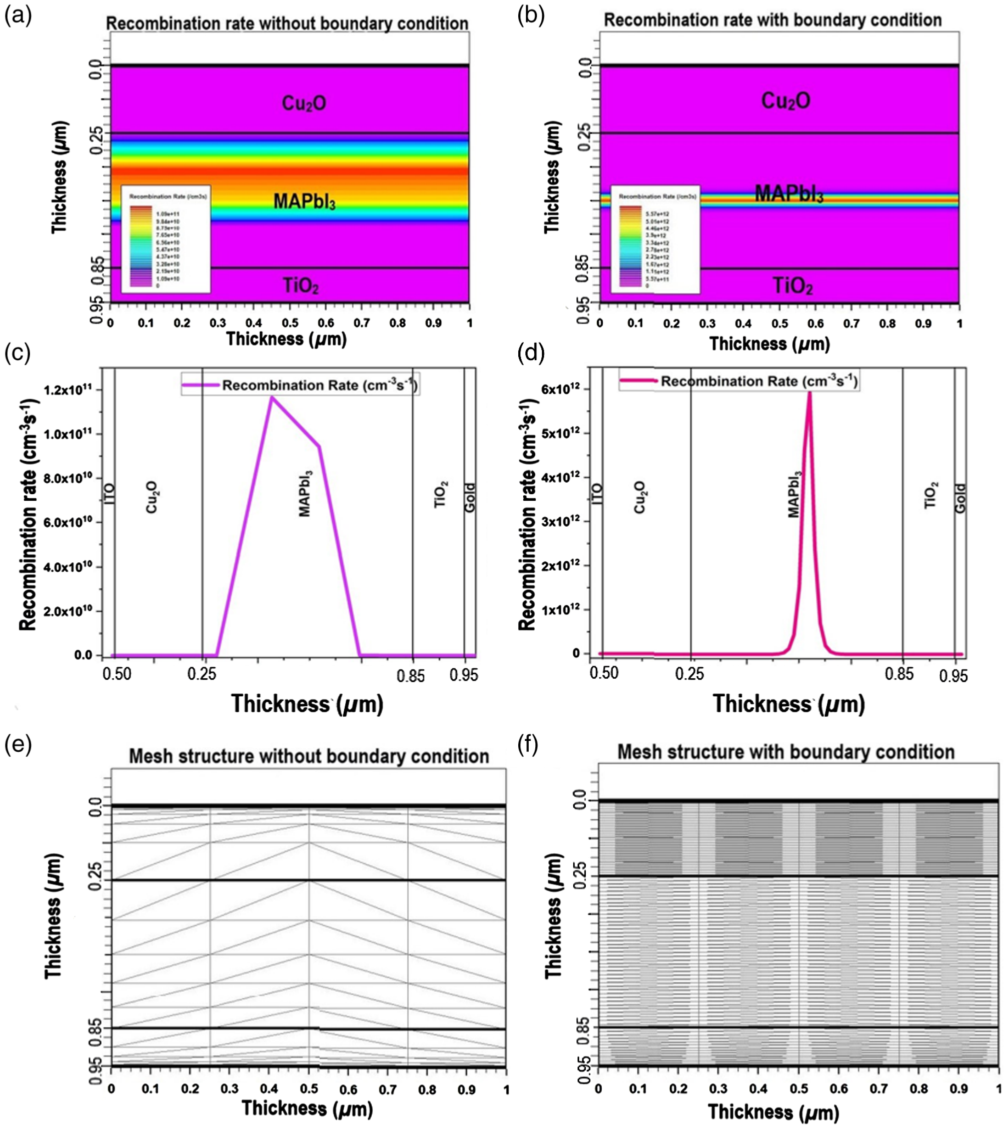

Fig. 2 Distribution of the recombination rate throughout the proposed PSC: (a) without boundary conditions and (b) with boundary conditions. The recombination rate throughout the proposed PSC: (c) without boundary conditions and (d) with boundary conditions. The mesh structure: (e) without boundary conditions and (f) with boundary conditions.

3.2 *Doping Effect*

The general descriptions of current density (J) and conductivity (σ) in a semiconductor, as applied in our simulation package, are presented in Eqs. (3)–(8), where n_n and p_n are the density of electrons and holes, respectively, and e and p are the electrical charges in a single electron and hole, respectively. μ_e is the electron mobility, μ_h is the hole mobility, and E denotes the applied electric field.[45]

$$J = (ne\mu_e + pe\mu_h)E, \tag{3}$$

$$\sigma = \frac{J}{E},\ \sigma - ne\mu_e + pe\mu_h, \tag{4}$$

$$J_n = e(n_n\mu_e + p_n\mu_n)E, \tag{5}$$

$$\sigma_n = e(n_n\mu_e + p_n\mu_h), \tag{6}$$

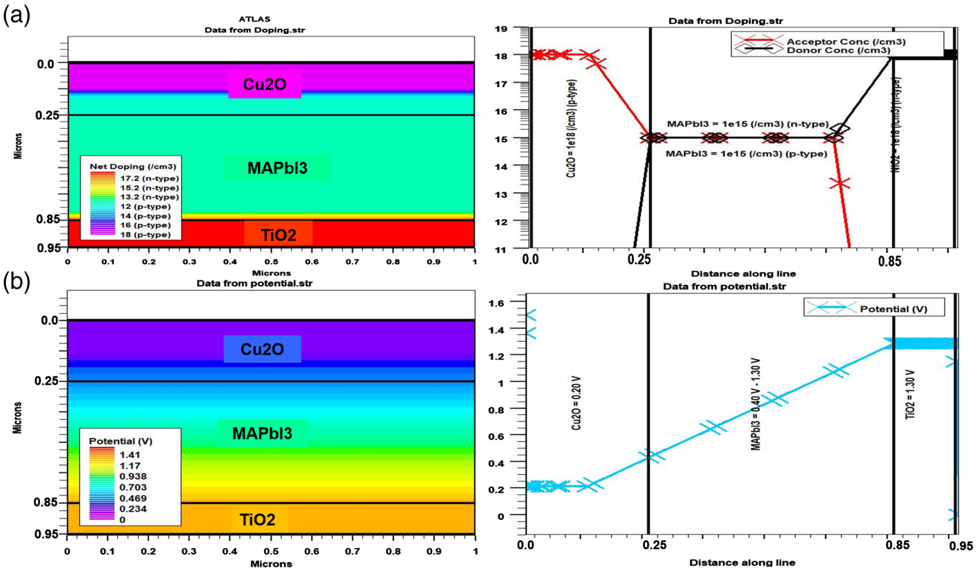

Fig. 3 (a) n-type and p-type doping distribution rate in different layers of the proposed structure (according to the graph, we observed the highest amount of acceptor concentration in the HTL, and the highest amount of donor concentration in ETL), and (b) potential distribution rate applied in different layers of the proposed structure (potential of 1.5 V was applied to the ETL).

$$J_p = e(n_p \mu_e + p_p \mu_h)E, \tag{7}$$

$$\sigma_p = e(n_p \mu_e + p_p \mu_h). \tag{8}$$

In the field of simulation, dopants or impurities mimic the carriers. The type and density of carriers are initially set as the tuning factors and optimized along with calculation cycles. Figures 3(a) and 3(b) show the doping and electrical potential distributions obtained for different layers of the designed PSC. The density of p-type carriers undergoes an upward trend from PV toward HTL, in which the p-type carriers are most frequent. The same trend is observed for n-type carriers from PV layer toward ETL as expected and perfectly accords with the real cases. In terms of electrical potential, simulation also follows the reality, whereby it remains at the minimum level in HTL and continuously increases linearly toward the PV part, to reach its maximum at the ETL border.

3.3 *Absorptance and Reflectance*

Light absorption capability is affected by both external and internal parameters, such as the intensity of incident photons, the area, and power of exposure, and the optical properties of the active layer. Moreover, depending on the side of exposure (back or front illumination), the intermediate layers such as the electrode and selective junction should be as transparent as possible and have a marginal reflecting effect, for a negligible parasitic absorption.[46–50] In this work, we theoretically characterized the absorption–reflectance behavior of the three main functional layers; ETL, HTL, and PV. The absorption coefficient of the PV layer is significantly higher than that of the selective layer, as expected, whereas the HTL is showing a higher absorption coefficient over the full wavelength (0 to 900 nm), as compared with the ETL. However, both selective layers possess a minor absorption coefficient along the full wavelength. On the other side, the reflectance of all mentioned layers was determined to be negligible [below 1%, Fig. 3(b)], making them desirable for efficient optical performance. With all these findings, it can be concluded that our proposed multijunction PSC is adequately designed for illumination of both sides (direct and inverted).

When a specific flux of incident photons (I) with an amount of energy, E, and intensity, I_0, collides with the surface of a solar cell, part of this flux is absorbed and reaches the photovoltaic layer. The portion of the incident light absorbed is influenced by various factors, including the travel distance of the photon (the thickness of the photovoltaic film, d_x, and the top layers) and the optical nature of photovoltaic materials [Eq. (9)]:

$$\frac{dI}{dx} = -\alpha I. \tag{9}$$

If we can assume that the energy of the absorbed photons is entirely consumed for creating the free charge carriers, the rate of generation can be denoted as

$$g(E, x) = b(E, x)\alpha(E, x), \tag{10}$$

where b is the photon flux along with x.

On the other hand, the rate of photon absorption depends on various parameters, such as the energy of quantum photons and the energy states of the absorption layer.[51–55] For absorption of photons, at least two levels of energy are required. To achieve a stable photon-to-charge function, the excited carrier's lifetime must be sufficiently greater than the time required for transmitting the carriers from the valance band to the conduction band. Also, a qualified photovoltaic material is evaluated based on its absorption coefficient (α), which is a function of the wavelength of incident photons, as denoted as[56–61]

$$\alpha = A(h\nu - E_g)^{\frac{1}{2}}, \tag{11}$$

where A is a constant, which is a function of the materials nature, $h\nu$ is the photon energy, and E_g is the bandgap of the material.

It should be noted that the intensity of the incident photons is exponentially varied during their passage through the different layers, according to

$$I = I_0 e^{-aX}. \tag{12}$$

There is always a share of reflected photons, which is defined as the ratio between the energy of the surface wave to the energy of the colliding wave to the surface. In other words, reflection is the refraction of a random light reflected from the surface, which is an intrinsic characteristic of materials. It is essential to determine the color characteristics, polarity, and transparency of materials.[62–64] Internal reflectance is another important phenomenon occurring in some optical devices. Figure 4 manifests that the incident rays and reflected photon rays have the same size of angles, as regards to the shared surface.

Reflectance is a function of the valance and conduction energy states of materials, which are intrinsic for each material and determined by the optical constants and the density of the free carriers on the surface. In general, the optical reflection trait of a material is indicated by the reflection index.

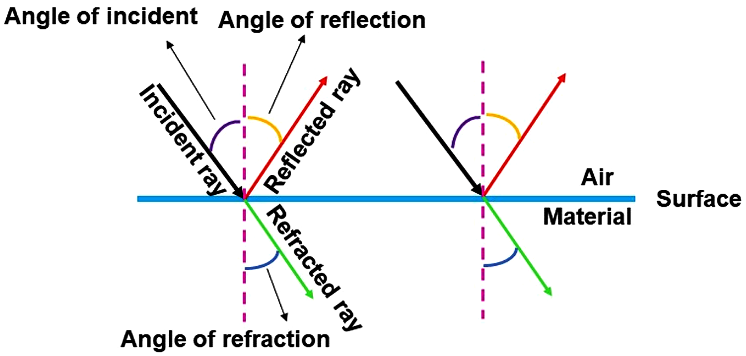

Fig. 4 The angles of the incident, reflected and refracted rays to the surface of the material.

$$n = n + iK, \tag{13}$$

where n denotes the surface reflective index, and K indicates the surface extinction coefficient. Beyond the materials, optical characters, position, and intensity of irradiation would profoundly dominate the optic-electronic activities.

Having known the details of influencing parameters, this study further envisages the effect of irradiation power on the photovoltaic efficiency of PSCs.

3.4 *Different Light Radiation Power*

For the optical investigation of this cell, the maximum absorption for different radiation powers was examined for the planar p-i-n perovskite device with a 600-nm-thick perovskite layer. Table 2 presents the output terms of this theoretical measurement and optimization. Figure 5(a) unveils that with a 1000-$\mathrm{W/m^2}$ radiation power, a minimum reflection occurs, as absorption increases significantly. However, Fig. 5(b) shows a serious drop of current density with a 1000-$\mathrm{W/m^2}$ radiation power. Such an observation could be because the higher powers of photon impact create further parasitic effects such as traps on the interfaces. As deduced from Figs. 5(a)–5(c) and Table 2, there should be a trade-off between the desired and adverse upshots of a reflectance power, which for the current case can be optimized when the power of irradiation is set at 1000 $\mathrm{W/m^2}$. $\mathrm{AM}_{1.5}$, 1.5-atmosphere thickness, matches a solar zenith angle of $z = 48$ deg. So, solar manufacturing has been using $\mathrm{AM}_{1.5}$ for all standardized measurement or rating of physical solar cells or modules, including those applied in concentrating systems.[65] For clarity, we can flashback to Fig. 4, which shows that normal refraction minimizes the potential of internal reflections and is associated with a higher chance of transmission.[66]

On the other hand, varying the radiation power in the range of 826 to 1000 $\mathrm{W/m^2}$ changes the effective light diffusion length. Such an interactive behavior states that illumination power should be optimized for each specific penetration thickness, including the thickness sizes of the front electrode (here; glass/ITO), the atop selective layer (here; $\mathrm{Cu_2O}$), and the active layer (perovskite).

Table 2 Photovoltaic parameters of various irradiation power, as calculated for the proposed p-i-n PSC.

Light power ($\mathrm{W/m^2}$)	*Voc* (V)	*Jsc* ($\mathrm{mA/cm^2}$)	*Vm* (V)	*Jm* ($\mathrm{mA/cm^2}$)	%FF	%PCE
1000	1.19	26.27	1.04	25.14	83.77	26.32
962	1.19	25.23	1.04	24.16	83.77	26.21
900	1.18	23.20	1.04	22.20	83.77	25.60
826	1.17	16.32	1.02	14.60	83.62	19.35

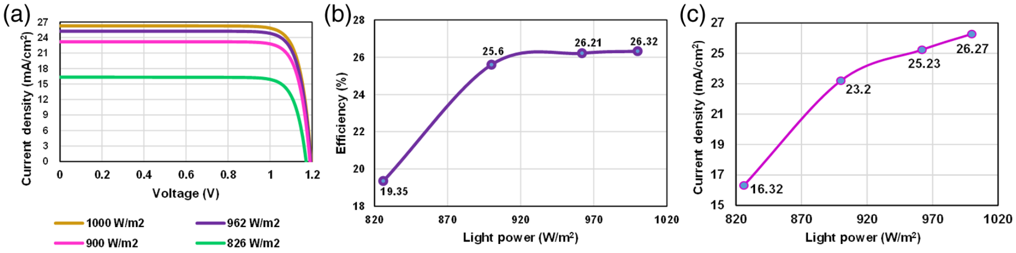

Fig. 5 (a) The *J–V* curve for the proposed PSC under different radiation powers, (b) the photovoltaic efficiency under different radiation powers, and (c) the cathode current density under different radiation powers.

Table 3 Comparison of the characteristic of the proposed structure with recent similar studies.

Reference	Light power (W/m^2)	%FF	%PCE
Giacomo et al.[67]	1000	77.00	15.90
Dagar et al.[68]	1000	75.70	19.00
Xu et al.[69]	1000	75.00	20.00
Tumen-Ulzii et al.[70]	1000	77.00	21.1
Patricia et al.[71]	1000	80.00	25.10
This work	**1000**	**83.77**	**26.32**

Results of this simulation under $AM_{1.5G}$ are very close to the state-of-art of experimental works (Table 3), with similar visions, proving the higher efficiency of this simulation method.

3.5 *Anode Buffer Layer*

The front selective layer (here; HTL) can also crucially affect the light-responses of the whole photovoltaic device. To survey this fact we ran a set of device simulations, based on different material systems for the front-side HTL. Figures 6(a)–6(d) and Table 4 briefly show the simulated external quantum efficiency (EQE), and PV metrics of the identical four planar p-i-n solar systems, utilizing different materials for the front selective layer. EQE is defined as the ratio between the electrons extracted from the device to the number of the incident light wavelength [Eq. (14)]. Here, we calculated the later parameters based on an optimum (48 deg) radiating power:

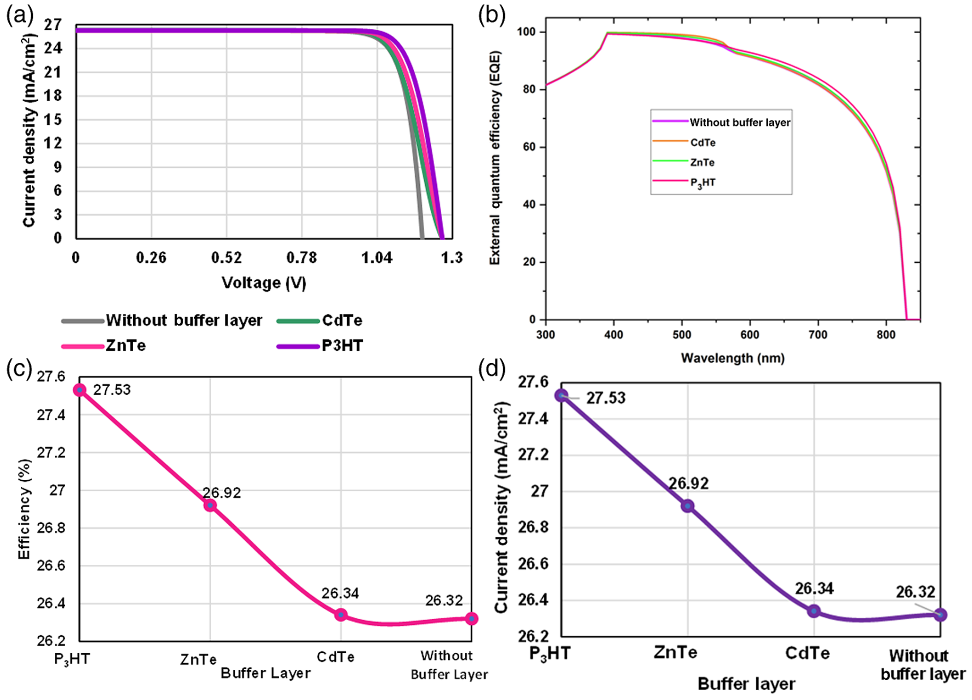

Fig. 6 (a) The influence of the anode buffer layer on the *J–V* curve. (b) The EQE curve for different anode buffer layers. (c) The impact of the anode buffer layer on efficiency. (d) The influence of the anode buffer layer on cathode current density.

Table 4 Output characteristics of the proposed PSC as influenced by the anode buffer layer materials.

Material	*Voc* (V)	*Jsc* (mA/cm^2)	*Vm* (V)	*Jm* (mA/cm^2)	%FF	% PCE
P_3HT	1.26	26.27	1.08	25.41	82.81	27.53
ZnTe	1.26	26.26	1.06	25.38	81.07	26.92
CdTe	1.26	26.25	1.04	25.37	79.77	26.34
Without buffer layer	1.19	26.27	1.04	25.14	83.77	26.32

$$\text{EQE} = \frac{\text{number of electrons out of device}}{\text{number of photons incident on device}}. \tag{14}$$

A minor difference in conversion and external quantum efficiencies is observed, and the best performance belongs to the cell that uses P_3HT, as HTL. The only variable parameters are the current density and FF. Current density is an indicator of the level of harvesting and generation, whereas FF is linked to the structure, which is in turn a function of the material nature. From a theoretical perspective, we may assume that P_3HT works better owing to a relatively better match of the energy states (work function, valance, and conduction bands) with the perovskite layer, and the same reason can be used for the comparatively poor performance of CdTe.[27,28,72] Overall, these findings may guide us to the fact that, if we can prepare a perfect stacking structure (in both crystalline and bulk scales), with an optimal thickness, the only remaining concern will be the energy state of the adopted materials.

Among the materials used as anode buffer layers, P_3HT is the best material due to the many advantages, such as high charge, easy synthesis, good processability, and carrier mobility.[73]

3.6 *Influence of HTL and ETL Thickness on Photovoltaic Performance*

As shown in Figs. 7(a)–7(c), the variation of the electron current density and efficiency with the thickness of HTL indicate a change in the series resistor. When the thickness of HTL increases from 100 to 500 nm, PCE decreases from 26.32% to 22.02% and corresponding cathode current density shifts from 26.27 to 26.49 mA/cm^2. Table 5 reveals that the most favorable photovoltaic function for the proposed outline is achieved when the thickness of HTL (based on Cu_2O) is set in the range of 100 to 500 nm. Such a prediction stands in line with reported theories and experiments, as a very thin active layer may fail in harvesting, and a very thick one causes a series of resistivity and imbalanced diffusion length.[3]

The HTL thickness of about 100 to 200 nm is ideal and suitable for high efficiency. Maximum *Jsc*, *Voc*, efficiency, and fill factor (FF) of 26.27 mA/cm^2, 1.19 V, 26.32%, and 83.77%, respectively, were obtained for a thickness of 200 nm. This result indicates less recombination in the device, an effective charge transport, high FF, low series resistance, and high FF.[74,75]

In the same line of thought, Figs. 8(a)–8(c) and Table 6 summarize the influence of ETL thickness (based on compact TiO_2), whereby the increase in the ETL thickness from 100 to 500 nm degrades both the overall cell efficiency and the current density from 26.32% to 25.99% and from 26.27 to 25.95 mA/cm^2, respectively. We accept this trend as a theoretical principle and connect it to the effect of series resistivity with increasing thickness of stacking. While in practice, further disturbing parameters such as the bulk and crystalline structure of ETL film and interfaces may rule out the trend.

When the ETL thickness increases, the case to restrict electron transport to ITO increases due to the higher recombination rate. This increases the series resistance to the solar cell, thus affecting efficiency and the FF. When the thickness of ETL increases, the electrons need to move a

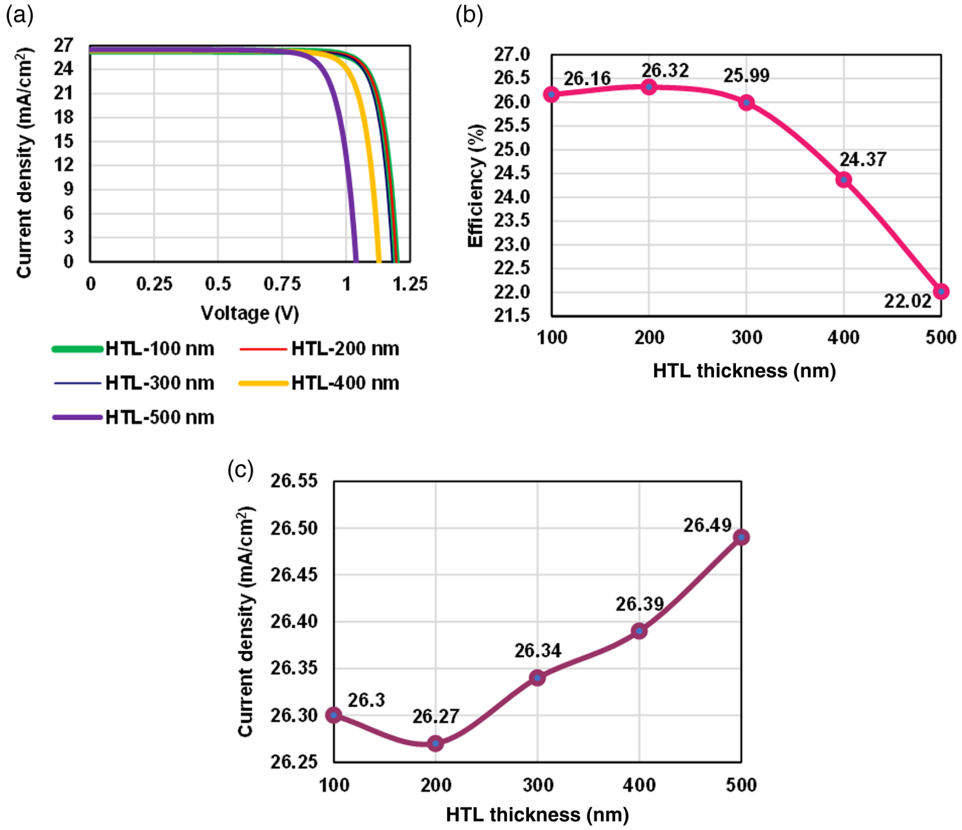

Fig. 7 (a) The *J*–*V* curve of the proposed structure with different HTL thickness, (b) the efficiency variation with different thickness of HTL, and (c) the cathode current density variation with different thickness of HTL (corresponding to Table 4).

Table 5 The proposed PSC characteristics with HTL thickness variations.

HTL thickness (nm)	*Voc* (V)	*Jsc* (mA/cm^2)	*Vm* (V)	*Jm* (mA/cm^2)	%FF	% PCE
100	1.19	26.30	1.04	25.05	83.30	26.16
200	1.19	26.27	1.04	25.14	83.77	26.32
300	1.17	26.34	1.03	25.11	83.63	25.99
400	1.12	26.39	0.97	25.01	81.90	24.37
500	1.03	26.49	0.88	24.96	80.04	22.02

long way to arrive at the top electrode. Due to a vast path distance, a high possibility for electrons to recombine exists with minority carriers. So, the PSC efficiency decreases significantly.[76,77]

3.7 *Influence of HTL and ETL Materials*

Figures 9(a) and 9(b) show the schematic energy state diagrams of different materials tested for ETL and HTL in the proposed perovskite cell.

Figures 10(a)–10(d) and Table 7 show the *J*–*V* trend and PV metrics, which were calculated for the designed PSC, based on $MAPbI_3$ (600 nm thickness), TiO_2 as ETL (100 nm thickness), and varying HTLs, i.e., Cu_2O, CuSCN, Spiro-OMeTAD, and P_3HT. It seems that Cu_2O as HTL yields the best operation for the proposed structure. This is further supported with the energy

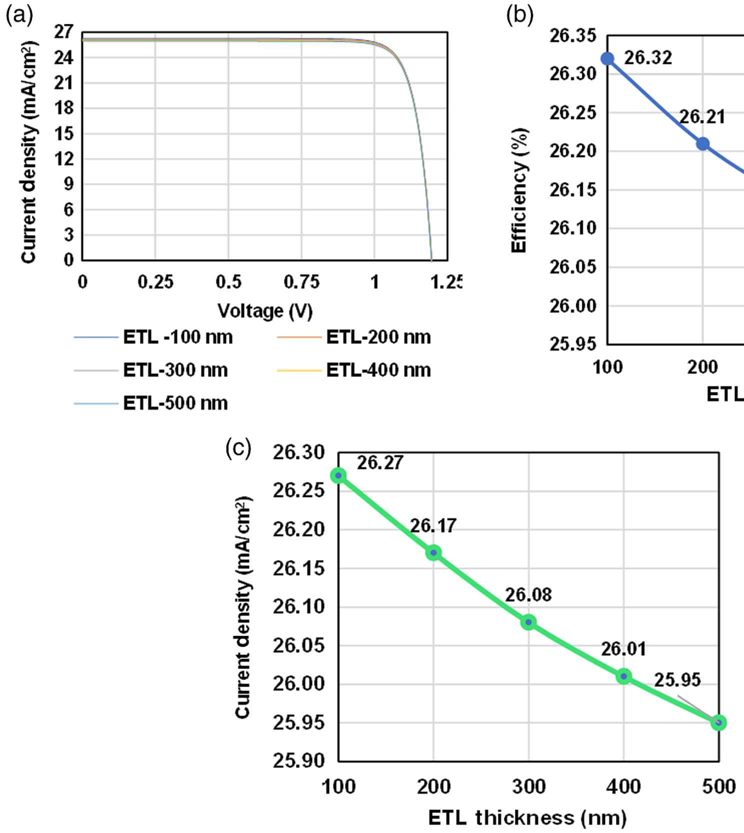

Fig. 8 (a) The *J*–*V* curve of the proposed structure with different ETL thickness, (b) the cathode current density variation with varying thicknesses of ETL, and (c) the efficiency variation with varying thicknesses of ETL (corresponding to Table 6).

Table 6 The proposed PSC characteristics with ETL thickness variations.

ETL thickness (nm)	*Voc* (V)	*Jsc* (mA/cm^2)	*Vm* (V)	*Jm* (mA/cm^2)	%FF	%PCE
100	1.19	26.27	1.04	25.13	83.77	26.32
200	1.19	26.17	1.04	25.04	83.77	26.21
300	1.19	26.08	1.04	24.96	83.77	26.13
400	1.19	26.01	1.04	24.89	83.77	26.05
500	1.19	25.95	1.04	24.83	83.77	25.99

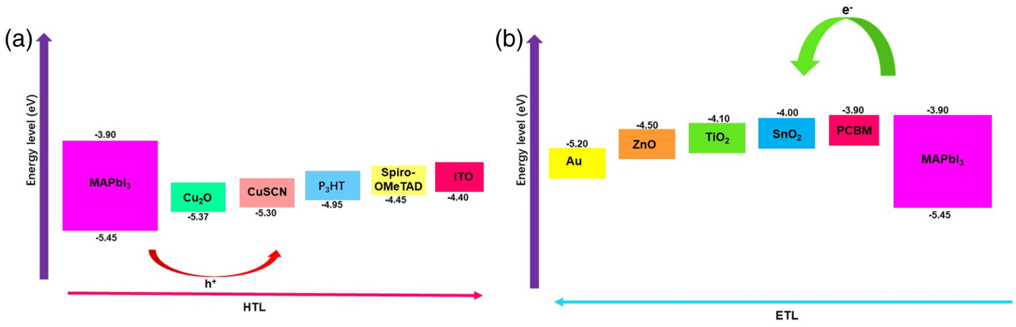

Fig. 9 The schematic energy state diagram of different materials, tested for (a) HTL and (b) ETL in the proposed perovskite cell.

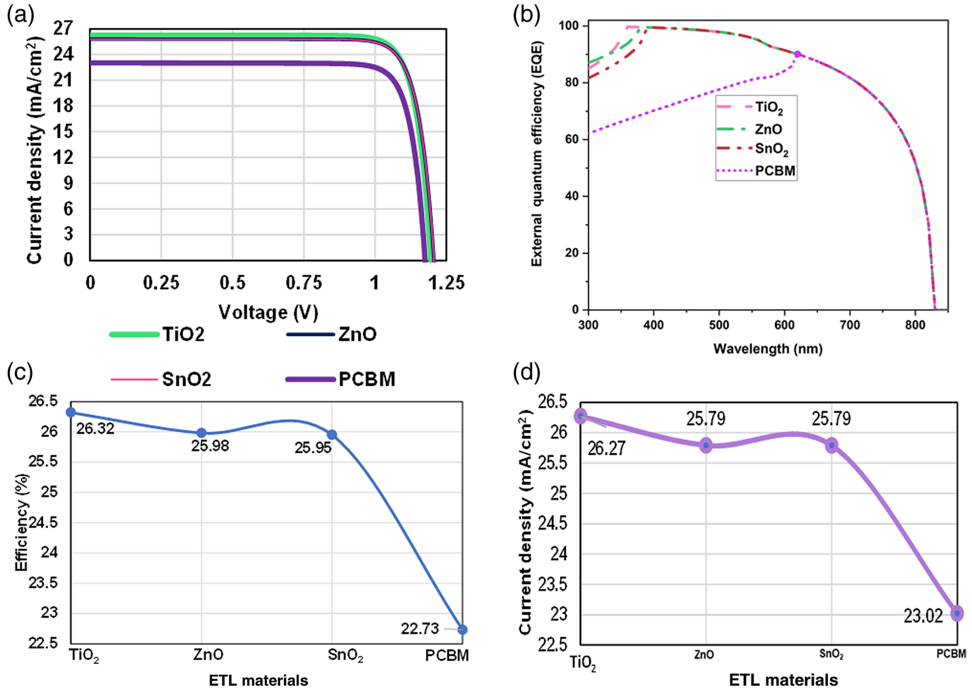

Fig. 10 (a) The *J–V* curve of PSC based on $MAPbI_3$, (b) the EQE for different HTL materials, (c) the efficiency for different HTL, and (d) the cathode current density for different HTL materials (corresponding to Table 8).

Table 7 The output parameters of the proposed structure with different HTL materials.

HTL materials	*Voc* (V)	*Jsc* (mA/cm²)	*Vm* (V)	*Jm* (mA/cm²)	%FF	%PCE
Cu_2O	1.19	26.27	1.04	25.14	83.77	26.32
Spiro-OMeTAD	1.17	26.24	1.00	25.33	84.23	26.02
P_3HT	1.16	26.24	0.96	25.35	83.82	25.52
CuSCN	1.11	26.35	1.02	25.28	83.06	25.50

state information in Fig. 9(a), where Cu_2O demonstrates the most desirable offset of valance band with $MAPbI_3$.

For this comparison, Cu_2O, Spiro-OMeTAD, P_3HT, and CuSCN were used as HTL. Because Cu_2O has a very high hole mobility rather than other selected materials, the hole mobility enhances the efficiency of the perovskite layer.[78]

Materials such as ZnO, SnO_2, PCBM, and TiO_2 were used as ETL layers, whereby TiO_2 portrayed the best efficiency because it exhibits a suitable band adjustment with the perovskite layer and a long electron lifetime, which decreases the hysteresis behavior of the PSCs.[79,80]

Similarly, Figs. 11(a) and 11(b) and Table 8 display the *J–V* trend and PV parameters of the designed PSC, versus the changes in ETL materials. The cell made of PCBM performs the minimum current density, EQE, and PCE, consequently. This operation may be due to the low electron and hole mobility of about 2.00×10^{-1}, which suppresses the acceleration of charge collection. On the other side, TiO_2 causes the best EQE and PCE. EQE, PCE, and the corresponding *Jsc* of four different cells, adopting different ETL materials are given in Figs. 11(b)–11(d).

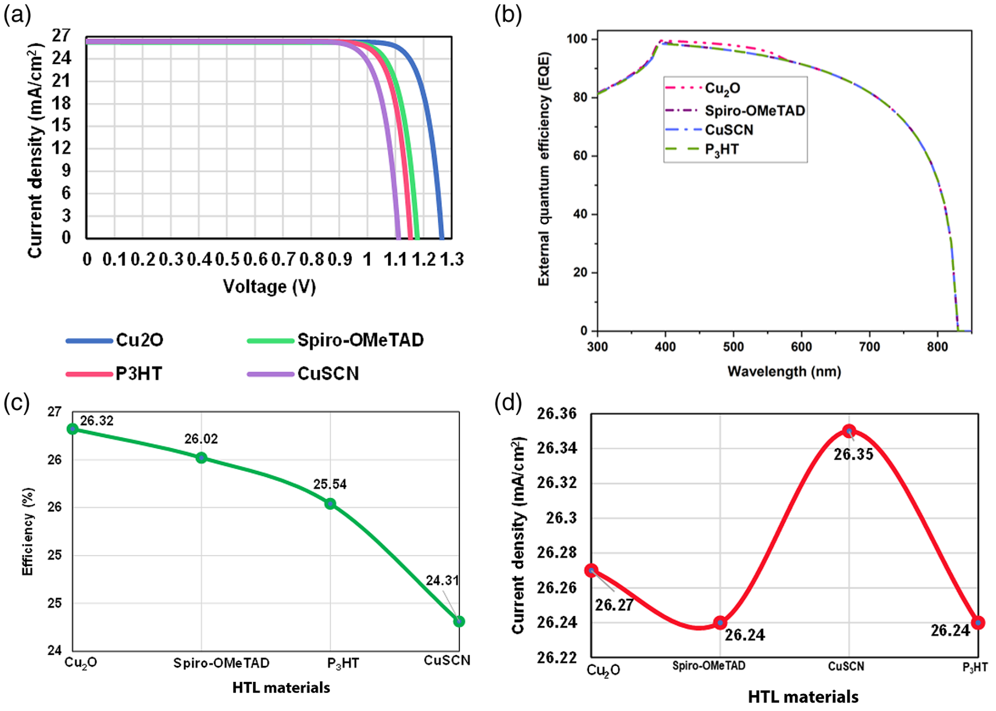

Fig. 11 (a) The *J*–*V* curve of PSC based on $\mathrm{MAPbI_3}$, (b) the EQE for different ETL materials, (c) the efficiency for different ETL, and (d) the cathode current density for different ETL materials.

Table 8 The output parameters of the proposed structure with different ETL materials.

ETL materials	*Voc* (V)	*Jsc* (mA/cm^2)	*Vm* (V)	*Jm* (mA/cm^2)	%FF	% PCE
TiO_2	1.19	26.27	1.04	25.14	83.77	26.32
ZnO	1.20	25.79	1.05	24.71	83.50	25.98
SnO_2	1.20	25.79	1.05	24.70	83.41	25.95
PCBM	1.17	23.02	1.03	22.01	84.00	22.73

4 Conclusion

Many studies have been previously conducted on PSCs, albeit with low PCE as compared with state-of-the-art silicon photovoltaics. In this work, we used two software programs, Silvaco and SCAPS, to demonstrate the influence of parameter variation on the proposed structure of PSCs. With the SCAPS software, we investigated the effect of ETL and HTL, the anode buffer layer materials, and the light radiation power on the proposed structure properties. With Silvaco, we calculated the optical properties of the proposed structure.

The simulation results revealed that the $\mathrm{MAPbI_3}$ PSC, with the HTL thickness of 100 nm and ETL thickness of 500 nm can generate a maximum cathode current density and efficiency by increasing the ETL and HTL thickness. We observed that the short-circuit current density and efficiency sharply decreased because of the increase in the series resistance. Moreover, by using suitable and new semiconductor materials as ETL and HTL of the PSC, PCE increases dramatically. We used different materials as the anode buffer layers and compared the results, whereby P_3HT turned out to be the best material for the anode buffer layer in the proposed structure. We also illuminated light with different radiation powers, and with 1000 $\mathrm{W/m^2}$, we obtained the maximum efficiency. After optimization of all the parameters, the *Voc*, *Jsc*, efficiency, and FF obtained were 1.19 V, 26.27 mA/cm^2, 26.32%, and 83.77%, respectively. This theoretical champion layout promises a feasible application of PSC as highly efficient electronic devices.

Acknowledgments

This work was supported by the Research Program of the School of Physics, Dalian University of Technology, China.

References

1. X. Zhang et al., "Highly efficient flexible perovskite solar cells made via ultrasonic vibration assisted room temperature cold sintering," *Chem. Eng. J.* **394**, 124887 (2020).
2. F. Zabihi et al., "Perovskite solar cell-hybrid devices: thermoelectrically, electrochemically, and piezoelectrically connected power packs," *J. Mater. Chem. A* **7**(47), 26661–26692 (2019).
3. B. Farhadi et al., "Highly efficient photovoltaic energy storage hybrid system based on ultrathin carbon electrodes designed for a portable and flexible power source," *J. Power Sour.* **422**, 196–207 (2019).
4. N. Mansour Rezaei Fumani et al., "Prolonged lifetime of perovskite solar cells using a moisture-blocked and temperature-controlled encapsulation system comprising a phase change material as a cooling agent," *ACS Omega* **5**(13), 7106–7114 (2020).
5. W. Chen et al., "A comparative study of planar and mesoporous perovskite solar cells with printable carbon electrodes," *J. Power Sour.* **412**, 118–124 (2019).
6. J. Jin et al., "Efficient and stable flexible perovskite solar cells based on graphene-AgNWs substrate and carbon electrode without hole transport materials," *J. Power Sour.* **482**, 228953 (2021).
7. L. Mao et al., "Chemical and structural diversity of hybrid layered double perovskite halides," *J. Am. Chem. Soc.* **141**(48), 19099–19109 (2019).
8. H. Xiong et al., "Grain engineering by ultrasonic substrate vibration post-treatment of wet perovskite films for annealing-free, high performance, and stable perovskite solar cells," *Nanoscale* **10**(18), 8526–8535 (2018).
9. F. Zabihi and M. Eslamian, "Low-cost transparent graphene electrodes made by ultrasonic substrate vibration-assisted spray coating (SVASC) for thin film devices," *Graphene Technol.* **2**(1-2), 1–11 (2017).
10. A. Balilonda et al., "Perovskite solar fibers: current status, issues and challenges," *Adv. Fiber Mater.* **1**, 101–125 (2019).
11. B. Farhadi et al., "A hypothesis on optoelectronic behavior of $CH_3NH_3SnI_xBr_{3-x}$ perovskite: density functional theory approach," *Solar Energy* **233**, 11–17 (2022).
12. N. Lakhdar and A. Hima, "Electron transport material effect on performance of perovskite solar cells based on $CH_3NH_3GeI_3$," *Opt. Mater.* **99**, 109517 (2020).
13. M. Chowdhury et al., "Effect of deep-level defect density of the absorber layer and n/i interface in perovskite solar cells by SCAPS-1D," *Results Phys.* **16**, 102839 (2020).
14. B. Farhadi et al., "Influence of contact electrode and light power on the efficiency of tandem perovskite solar cell: numerical simulation," *Solar Energy* **226**, 161–172 (2021).
15. S. Malyukov, A. Sayenko, and A. Ivanova, "Numerical modeling of perovskite solar cells with a planar structure," in *IOP Conf. Ser.: Mater. Sci. and Eng.*, IOP Publishing (2016).
16. A. Toshniwal et al., "Numerical simulation of tin based perovskite solar cell: effects of absorber parameters and hole transport materials," *J. Nano Electron. Phys.* **9**(3), 03038 (2017).
17. S. Rai, B. Pandey, and D. Dwivedi, "Modeling of highly efficient and low cost $CH_3NH_3Pb(I_{1-x}Cl_x)_3$ based perovskite solar cell by numerical simulation," *Opt. Mater.* **100**, 109631 (2020).
18. B. Farhadi et al., "Carbon doped lead-free perovskite with superior mechanical and thermal stability," *Mol. Phys.* e2013555 (2021).

19. M. Jamal et al., “Effect of defect density and energy level mismatch on the performance of perovskite solar cells by numerical simulation,” *Optik* **182**, 1204–1210 (2019).
20. R. R. Kumar and S. K. Pandey, “Performance evaluation and material parameter perspective of eco-friendly highly efficient $CsSnGeI_3$ perovskite solar cell,” *Superlattices Microstruct.* **135**, 106273 (2019).
21. F. Di Giacomo et al., “Progress, challenges and perspectives in flexible perovskite solar cells,” *Energy Environ. Sci.* **9**(10), 3007–3035 (2016).
22. X. Xu et al., “Thermally stable, highly efficient, ultraflexible organic photovoltaics,” *Proc. Natl. Acad. Sci. U. S. A.* **115**(18), 4589–4594 (2018).
23. A. Polman et al., “Photovoltaic materials: present efficiencies and future challenges,” *Science* **352**(6283), aad4424 (2016).
24. A. Pivrikas et al., “A review of charge transport and recombination in polymer/fullerene organic solar cells,” *Prog. Photovoltaics: Res. Appl.* **15**(8), 677–696 (2007).
25. P. Docampo et al., “Lessons learned: from dye-sensitized solar cells to all-solid-state hybrid devices,” *Adv. Mater.* **26**(24), 4013–4030 (2014).
26. M. A. Green, A. Ho-Baillie, and H. J. Snaith, “The emergence of perovskite solar cells,” *Nat. Photonics* **8**(7), 506–514 (2014).
27. F. Azri et al., “Electron and hole transport layers optimization by numerical simulation of a perovskite solar cell,” *Solar Energy* **181**, 372–378 (2019).
28. S. Abdelaziz et al., “Investigating the performance of formamidinium tin-based perovskite solar cell by SCAPS device simulation,” *Opt. Mater.* **101**, 109738 (2020).
29. N. Bochra and B. Abdelhak, “Characterization of InGaN solar cells,” *J. Mater. Sci. Chem. Eng.* **3**(11), 88–91 (2015).
30. M. Kaifi and S. Gupta, “Simulation of perovskite based solar cell and photodetector using SCAPS software,” *Int. J. Eng. Res. Technol.* **10**(12), 1778–1786 (2019).
31. D. Liu, M. K. Gangishetty, and T. L. Kelly, “Effect of $CH_3NH_3PbI_3$ thickness on device efficiency in planar heterojunction perovskite solar cells,” *J. Mater. Chem. A* **2**(46), 19873–19881 (2014).
32. M. Kulbak et al., “Cesium enhances long-term stability of lead bromide perovskite-based solar cells,” *J. Phys. Chem. Lett.* **7**(1), 167–172 (2016).
33. J. Berry et al., “Hybrid organic–inorganic perovskites (HOIPs): opportunities and challenges,” *Adv. Mater.* **27**(35), 5102–5112 (2015).
34. H. Cho et al., “Overcoming the electroluminescence efficiency limitations of perovskite light-emitting diodes,” *Science* **350**(6265), 1222–1225 (2015).
35. H. Wei et al., “Sensitive x-ray detectors made of methylammonium lead tribromide perovskite single crystals,” *Nat. Photonics* **10**(5), 333–339 (2016).
36. G. Xing et al., “Low-temperature solution-processed wavelength-tunable perovskites for lasing,” *Nat. Mater.* **13**(5), 476–480 (2014).
37. M. Yuan et al., “Perovskite energy funnels for efficient light-emitting diodes,” *Nat. Nanotechnol.* **11**(10), 872–877 (2016).
38. W.-J. Yin, T. Shi, and Y. Yan, “Unusual defect physics in $CH_3NH_3PbI_3$ perovskite solar cell absorber,” *Appl. Phys. Lett.* **104**(6), 063903 (2014).
39. Q. Wang et al., “Qualifying composition dependent p and n self-doping in $CH_3NH_3PbI_3$,” *Appl. Phys. Lett.* **105**(16), 163508 (2014).
40. S. De Wolf et al., “Organometallic halide perovskites: sharp optical absorption edge and its relation to photovoltaic performance,” *J. Phys. Chem. Lett.* **5**(6), 1035–1039 (2014).
41. J. Wang et al., “Exciton blocking and dissociation by a p-type anode buffer in small molecule bulk heterojunction organic photovoltaic with small ratio donor of phosphorescent material,” *Org. Electron.* **23**, 11–16 (2015).
42. X. Feng et al., “Nano/micro-structured silicon@carbon composite with buffer void as anode material for lithium ion battery,” *Ceram. Int.* **42**(1), 589–597 (2016).
43. Z. Yu et al., “An aqueous solution-processed CuOX film as an anode buffer layer for efficient and stable organic solar cells,” *J. Mater. Chem. A* **4**(14), 5130–5136 (2016).
44. M. G. Varnamkhasti et al., “Comparison of metal oxides as anode buffer layer for small molecule organic photovoltaic cells,” *Solar Energy Mater. Solar Cells* **98**, 379–384 (2012).

45. P. Lopez-Varo et al., “Physical aspects of ferroelectric semiconductors for photovoltaic solar energy conversion,” *Phys. Rep.* **653**, 1–40 (2016).
46. D. K. Jarwal et al., “Fabrication and TCAD simulation of TiO_2 nanorods electron transport layer based perovskite solar cells,” *Superlattices Microstruct.* **140**, 106463 (2020).
47. Q. Duan et al., “Design of hole-transport-material free $CH_3NH_3PbI_3/CsSnI_3$ all-perovskite heterojunction efficient solar cells by device simulation,” *Solar Energy* **201**, 555–560 (2020).
48. X. Gonze et al., “The ABINIT project: impact, environment and recent developments,” *Comput. Phys. Commun.* **248**, 107042 (2020).
49. M. Y. Ameen et al., “MoO_3 anode buffer layer for efficient and stable small molecular organic solar cells,” *Opt. Mater.* **39**, 134–139 (2015).
50. L. Bertoluzzi et al., “Mobile ion concentration measurement and open-access band diagram simulation platform for halide perovskite solar cells,” *Joule* **4**(1), 109–127 (2020).
51. Y. Kawano et al., “Influence of halogen content in mixed halide perovskite solar cells on cell performances through device simulation,” *Solar Energy Mater. Solar Cells* **205**, 110252 (2020).
52. J. Madan et al., “Numerical simulation of charge transport layer free perovskite solar cell using metal work function shifted contacts,” *Optik* **202**, 163646 (2020).
53. R. Pandey and R. Chaujar, “Numerical simulations: toward the design of 27.6% efficient four-terminal semi-transparent perovskite/SiC passivated rear contact silicon tandem solar cell,” *Superlattices Microstruct.* **100**, 656–666 (2016).
54. T. Minemoto et al., “Numerical reproduction of a perovskite solar cell by device simulation considering band gap grading,” *Opt. Mater.* **92**, 60–66 (2019).
55. S. Zandi and M. Razaghi, “Finite element simulation of perovskite solar cell: a study on efficiency improvement based on structural and material modification,” *Solar Energy* **179**, 298–306 (2019).
56. G. Casas et al., “Analysis of the power conversion efficiency of perovskite solar cells with different materials as hole-transport layer by numerical simulations,” *Superlattices Microstruct.* **107**, 136–143 (2017).
57. N. Shahverdi et al., “Optimization of anti-reflection layer and back contact of perovskite solar cell,” *Solar Energy* **189**, 111–119 (2019).
58. J. You et al., “Moisture assisted perovskite film growth for high performance solar cells,” *Appl. Phys. Lett.* **105**(18), 183902 (2014).
59. D. Bryant et al., “A transparent conductive adhesive laminate electrode for high-efficiency organic-inorganic lead halide perovskite solar cells,” *Adv. Mater.* **26**(44), 7499–7504 (2014).
60. F. Hao et al., “Lead-free solid-state organic–inorganic halide perovskite solar cells,” *Nat. Photonics* **8**(6), 489–494 (2014).
61. B. Suarez et al., “Recombination study of combined halides (Cl, Br, I) perovskite solar cells,” *J. Phys. Chem. Lett.* **5**(10), 1628–1635 (2014).
62. S. Aharon, B. E. Cohen, and L. Etgar, “Hybrid lead halide iodide and lead halide bromide in efficient hole conductor free perovskite solar cell,” *J. Phys. Chem. C* **118**(30), 17160–17165 (2014).
63. C. Chen et al., “Efficient perovskite solar cells based on low-temperature solution-processed $(CH_3NH_3)PbI_3$ perovskite$/CuInS_2$ planar heterojunctions,” *Nanoscale Res. Lett.* **9**(1), 457 (2014).
64. M. Sittirak et al., “The effects of layer thickness and charge mobility on performance of FAI:MABr$:PbI_2:PbBr_2$ perovskite solar cells: GPVDM simulation approach,” in *J. Phys.: Conf. Ser.*, IOP Publishing (2019).
65. C. A. Gueymard, D. Myers, and K. Emery, “Proposed reference irradiance spectra for solar energy systems testing,” *Solar Energy* **73**(6), 443–467 (2002).
66. Q. Sun et al., “Highly sensitive terahertz thin-film total internal reflection spectroscopy reveals in situ photoinduced structural changes in methylammonium lead halide perovskites,” *J. Phys. Chem. C* **122**(30), 17552–17558 (2018).
67. F. Di Giacomo et al., “Mesoporous perovskite solar cells and the role of nanoscale compact layers for remarkable all-round high efficiency under both indoor and outdoor illumination,” *Nano Energy* **30**, 460–469 (2016).

68. J. Dagar et al., “Highly efficient perovskite solar cells for light harvesting under indoor illumination via solution processed SnO_2/MgO composite electron transport layers,” *Nano Energy* **49**, 290–299 (2018).
69. X. Xu et al., “A power pack based on organometallic perovskite solar cell and supercapacitor,” *ACS Nano* **9**(2), 1782–1787 (2015).
70. G. Tumen-Ulzii et al., “Detrimental effect of unreacted PbI_2 on the long-term stability of perovskite solar cells,” *Adv. Mater.* **32**(16), 1905035 (2020).
71. P. S. Schulze et al., “25.1% high-efficiency monolithic perovskite silicon tandem solar cell with a high bandgap perovskite absorber,” *Solar RRL* **4**(7), 2000152 (2020).
72. L. Lin et al., “Simulated development and optimized performance of $CsPbI_3$ based all-inorganic perovskite solar cells,” *Solar Energy* **198**, 454–460 (2020).
73. H.-J. Wang, C.-P. Chen, and R.-J. Jeng, “Polythiophenes comprising conjugated pendants for polymer solar cells: a review,” *Materials* **7**(4), 2411–2439 (2014).
74. A. Bag et al., “Effect of absorber layer, hole transport layer thicknesses, and its doping density on the performance of perovskite solar cells by device simulation,” *Solar Energy* **196**, 177–182 (2020).
75. C. Y. Chang, B. C. Tsai, and Y. C. Hsiao, “Efficient and stable vacuum-free-processed perovskite solar cells enabled by a robust solution-processed hole transport layer,” *ChemSusChem* **10**(9), 1981–1988 (2017).
76. N. Rai et al., “Analysis of various ETL materials for an efficient perovskite solar cell by numerical simulation,” *J. Mater. Sci.: Mater. Electron.* **31**(19), 16269–16280 (2020).
77. R. Jeyakumar et al., “Influence of electron transport layer (TiO_2) thickness and its doping density on the performance of $CH_3NH_3PbI_3$-based planar perovskite solar cells,” *J. Electron. Mater.* **49**, 3533–3539 (2020).
78. J. A. Owolabi et al., “Investigating the effect of ZnSe (ETM) and Cu_2O (HTM) on absorber layer on the performance of pervoskite solar cell using SCAPS-1D,” *Am. J. Phys. Appl.* **8**(1), 8–18 (2020).
79. N. J. Jeon et al., “Solvent engineering for high-performance inorganic–organic hybrid perovskite solar cells,” *Nat. Mater.* **13**(9), 897–903 (2014).
80. S. K. Pathak et al., “Performance and stability enhancement of dye-sensitized and perovskite solar cells by Al doping of TiO_2,” *Adv. Funct. Mater.* **24**(38), 6046–6055 (2014).

Biographies of the authors are not available.